FRAMEWORK MATERIALS

The propensity for covalent organic frameworks to template polymer entanglement

S. Ephraim Neumann[1,2]†, Junpyo Kwon[3,4]†, Cornelius Gropp[1,2], Le Ma[4,5], Raynald Giovine[1], Tianqiong Ma[1,2], Nikita Hanikel[1,2], Kaiyu Wang[1,2], Tiffany Chen[1,4], Shaan Jagani[5], Robert O. Ritchie[3,4,5]*, Ting Xu[1,2,4,5]*, Omar M. Yaghi[1,2,6]*

The introduction of molecularly woven three-dimensional (3D) covalent organic framework (COF) crystals into polymers of varying types invokes different forms of contact between filler and polymer. Whereas the combination of woven COFs with amorphous and brittle polymethyl methacrylate results in surface interactions, the use of the liquid-crystalline polymer polyimide induces the formation of polymer-COF junctions. These junctions are generated by the threading of polymer chains through the pores of the nanocrystals, thus allowing for spatial arrangement of polymer strands. This offers a programmable pathway for unthreading polymer strands under stress and leads to the in situ formation of high-aspect-ratio nanofibrils, which dissipate energy during the fracture. Polymer-COF junctions also strengthen the filler-matrix interfaces and lower the percolation thresholds of the composites, enhancing strength, ductility, and toughness of the composites by adding small amounts (~1 weight %) of woven COF nanocrystals. The ability of the polymer strands to closely interact with the woven framework is highlighted as the main parameter to forming these junctions, thus affecting polymer chain penetration and conformation.

Polymer chain entanglements help govern polymer structure-property relations and affect their mechanical properties (*1*, *2*). Modulation of polymer entanglements can be achieved with fillers such as carbon black, silica gels, and other types of nanoparticles (*3*–*5*), as well as through interpenetrating networks (*6*, *7*), supramolecular hosts (*8*), polymer-grafted nanoparticles (*9*, *10*), and nanoconfinement (*11*). In all cases, an increase in entanglement density leads to additional pathways to dissipate energy under stress. For example, polymer-grafted nanoparticles can control the directionality and local density of entanglements, resulting in crazing during stress (*12*, *13*). Major advancements have been made by improving the network perfection in gels, which differ from polymer solids forming the basis for most plastic products (*14*, *15*).

When polymers are threaded through porous structures such as metal organic frameworks (MOFs) and covalent organic frameworks (COFs), the crystalline order of the frameworks has the potential to template the spatial arrangements of polymer chains, offering pathways for unthreading under stress. This changes the modes of how composites dissipate energy during fracture from being largely by bond rupture to long-chain pull-out and extension at such junctions (Fig. 1). We hypothesize that the mechanical and chemical similarity of the woven COF backbone to the polymer matrix will result in a more homogeneous interface compared with other MOFs and COFs. Because each COF nanocrystal can template numerous polymer chains, the pulled-out chains form high-aspect-ratio nanofibrils under stress in situ, resulting in macroscopically improved damage tolerance in polymer-COF composites in the form of strength, ductility, and improved resistance to fracture (toughness).

In the blends of polymer and COF nanocrystals (Fig. 1A), hundreds of polymer chains are templated with periodic control when the polymer-COF junctions are formed. The polymer segments extending from their surfaces enhance the solubility of COF nanocrystals for better dispersion (Fig. 1B) and strengthen the filler-matrix interface by bridging the woven COF particles and the matrix. At the molecular level, the threaded polymers within the COF units are analogous to polymer-polymer junctions (*16*) but could offer the reversibility of the entanglements of the polymer. By forming polymer-COF junctions, there is no need to chemically cross-link the host polymer to enhance mechanical properties, and the blends are more amenable to recycling (*17*). Fundamentally atomically defined, crystalline COF networks can realize topological control over polymer entanglements, probing the spatial arrangements of a long chain at the molecular level (*18*).

Nonetheless, COF nanocrystals have the potential to act as classical nanoparticle fillers, wherein the polymer may mainly interact with the surface instead of threading through the framework (Fig. 1A). We studied the inclusion of molecular woven (MW) amide-based COFs into two polymer systems that were selected to delineate the effects of these nanoparticles. Polymethyl methacrylate (PMMA), being amorphous and brittle, does not strongly interact with COFs, so it can be used to investigate whether the polymer chains can thread through pores defined by the nanoporous COF filler. Polyimide (PI) was selected for multiple reasons. First, it is chemically similar to the backbone of the COFs, and their favorable interactions ensure in-depth penetration into the framework. Second, PI exhibits strong intra- and intermolecular interactions, and its macroscopic properties rely on these interactions over a long range. Finally, once PI is incorporated into COF nanoparticles, the framework will template its chain conformation and modulate the range of intermolecular interactions. The latter facilitates the formation of high-aspect-ratio nanofibers without compromising the global mechanical property.

In both cases, we observed the formation of extended nanofibrils after tensile testing. However, PI threads through the MW nanocrystals, whereas PMMA mainly forms surface contacts, which coincides with greater nanofibril extension for PI than PMMA and is reflected in the mechanical enhancement of PI-COF composites. Our spectroscopy studies were able to distinguish between these cases and offer an understanding of both types of interactions with woven organic nanoparticles.

Factors governing COF-polymer entanglement

Here, we tested these hypotheses by blending COF nanocrystals (0.5 to 5 wt %) with liquid crystalline polymers. Upon mechanical deformation, numerous high-aspect-ratio nanofibrils form at the fracture surface as a result of the unthreading of polymers from COF nanocrystals under stress (Fig. 1C). The effect of the polymer-COF junction extends beyond COF nanocrystal-matrix interfaces because the blends can effectively dissipate energy uniformly. This leads to enhancements in strength, ductility, and toughness, thus conferring damage tolerance. Polymer-COF junction formation is entropy driven and governed by polymer chain conformation. At the molecular level, the penetration depth and conformation of the polymer inside of COF crystals, the topology of polymer-COF junctions, and the morphology of polymer nanofibrils all depend on the COF crystal structure. This reflects a balance between the statistical contribution

[1]Department of Chemistry, University of California-Berkeley, Berkeley, CA 94720, USA. [2]Kavli Energy NanoSciences Institute, Berkeley, CA 94720, USA. [3]Department of Mechanical Engineering, University of California-Berkeley, Berkeley, CA 94720, USA. [4]Materials Science Division, Lawrence Berkeley National Laboratory, Berkeley, CA 94720, USA. [5]Department of Materials Science & Engineering, University of California-Berkeley, Berkeley, CA 94720, USA. [6]Bakar Institute of Digital Materials for the Planet, Division of Computing, Data Science, and Society, University of California-Berkeley, Berkeley, CA 94720, USA.
***Corresponding author. Email: roritchie@lbl.gov (R.O.R.); tingxu@berkeley.edu (T.X.); yaghi@berkeley.edu (O.M.Y.)**
†These authors contributed equally to this work.

of the torsion angle distribution for a polymer chain and the geometric constraints imposed by each COF unit cell.

Selection of COF nanocrystals

Nanocrystals of COFs and MOFs, including COF-500 (*19*), COF-506 (*20*, *21*), COF-300 (*22*), COF-791 (*23*), MOF-808 (*24*), and MIL-53 (*25*), were tested. Prior studies on the effect of mechanical bonding in polymers involved mechanically interlocked molecules such as rotaxanes and catenanes (*26*–*28*). Here, we chose to work with molecularly defined, porous, woven three-dimensional (3D) nanocrystals. Molecular weaving was first reported in imine-linked COF-505 and COF-506 (*29*, *30*). Imine linkages can generate crystalline extended structures but generally lack chemical stability (*31*). Therefore, we oxidized the imine linkages postsynthetically to form the more resilient amide-linked COF-507, referred to as MW COF (*32*) (see the supplementary materials). Powder x-ray diffraction analysis confirmed the crystallinity of the resulting woven amide-linked COF (see the supplementary materials, section S2). Fourier-transform infrared spectroscopy showed the disappearance of the characteristic imine bond stretch at 1622 cm^{-1} and the emergence of the amide carbonyl stretch at 1666 cm^{-1} (see the supplementary materials, section S3). The amide linkage was further confirmed by solid-state nuclear magnetic resonance (NMR) spectroscopy of ^{13}C-isotope enriched COFs, in which the isotopically enriched carbon was positioned within the imine and amide linkages (see the supplementary materials, section S4). Scanning electron microscopy (SEM) characterization showed COF crystallites with an average size of 300 to 400 nm (Fig. 2A and see the supplementary materials, section S5), and thermogravimetric analysis confirmed their thermal stability at processing temperatures of at least 300°C (see the supplementary materials, section S6).

PMMA-COF composites

Initially, we selected amorphous and brittle PMMA to test whether polymer-COF junctions could form and if these interactions enhance the ductility of the PMMA-COF composites. MW nanocrystals (3 wt %) were introduced to PMMA with a number-averaged molecular weight (M_n) of 535.5 kDa and a polydispersity index (PDI) of 2.50 by solution mixing. Transmission electron microscopy (TEM) imaging confirmed that the MW nanocrystals were well dispersed in the PMMA matrix (Fig. 2B).

Uniaxial mechanical tensile tests at ambient temperature showed that the fracture strain of the PMMA-MW composites (3 wt %) increased from 0.13 (±0.02) to 0.22 (±0.04) mm/mm (n = 5). The toughness, determined by the area under the engineering stress-strain curves, nearly doubled from 2.6 (±0.5) MPa in the pure PMMA to 5.6 (±1.4) MPa in PMMA-MW (3 wt %) (Fig. 2C). We performed additional fracture tests using double-notch specimens consisting of rectangular films with two nominally identical notches to characterize critical events before the onset of final failure (*33*, *34*). Because both notches experienced the same stress and displacement fields, when one notch fractured, the unfractured notch became the point of fracture and thus could provide evidence of the precursor events just before unstable fracture.

SEM images showed that the fracture surfaces in PMMA-MW exhibited high surface roughness and the formation of a few nanofibrils that bridged the cracks (Fig. 2D). The dimensions of the fibrils were 1.5 (±0.9) μm in length (n > 10 samples) and 0.3 (±0.1) μm in diameter with an aspect ratio ($\lambda_{PMMA\text{-}MW}$) of 5.35 (±3.97). This λ value was about twice that commonly reported for glassy polymers such as PMMA (λ_{PMMA} ~2.55) (*35*, *36*). The observed polymer nanofibrils suggest that the PMMA chains, through their interaction with MW nanocrystals, were stretched and aligned more readily to dissipate energy under stress.

We used wide-angle x-ray scattering (WAXS) to investigate the crystal structure of the embedded COF nanocrystals (Fig. 2E). Compared with the characteristic diffraction peaks for the pristine MW, the peaks from the MW COF crystals embedded in PMMA shifted to slightly lower values of the scattering vector q. This difference suggests that the PMMA chains may penetrate the pores of the woven

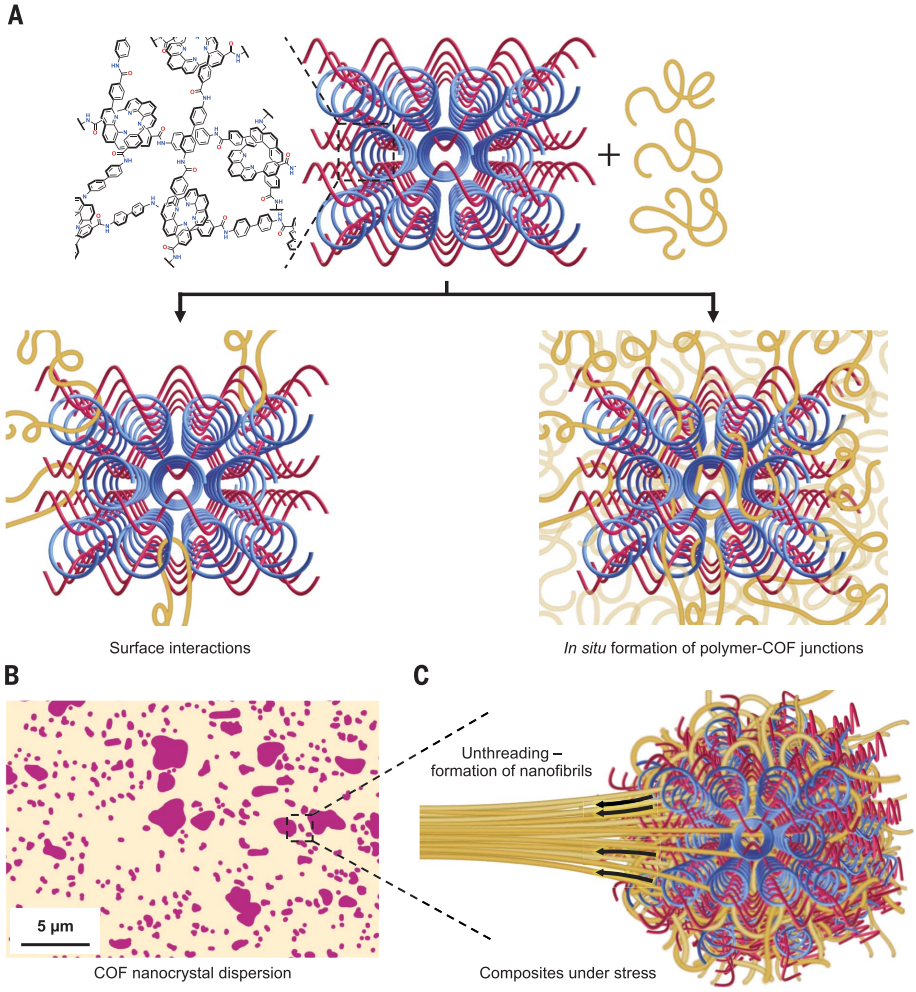

Fig. 1. Schematic illustration of the COF structure, polymers, and nanofibrils. (**A**) Polymer-COF interactions. Depending on the polymer, its matrix may either interface only with the surface of the woven COF particles or form so-called polymer-COF junctions. In these junctions, individual polymer chains penetrate the porous, 3D woven COF crystals and decorate the surface to interact with the polymer matrix. (**B**) COF nanocrystals distributed nanoscopically without any necessary surface modification to enhance compatibility. (**C**) Polymer-COF composites under stress. The polymer chains spatially align and unthread from the COF crystals, thereby generating a favorable pathway for energy dissipation and forming nanofibrils.

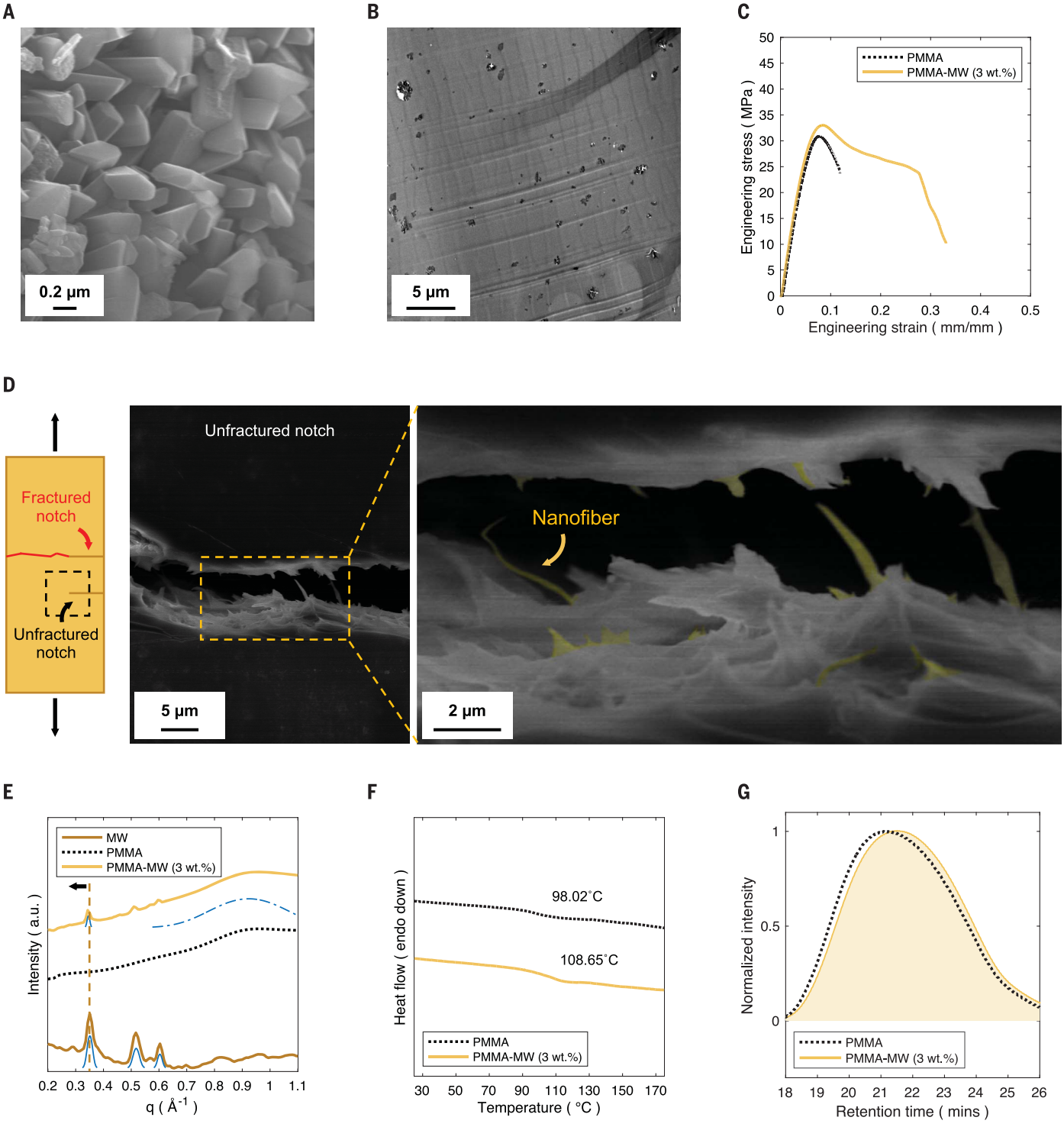

Fig. 2. Characterization of PMMA-COF composites. (**A**) SEM micrograph of MW nanocrystals. (**B**) TEM image of PMMA-MW (3 wt %) showing well-dispersed MW nanocrystals in the PMMA matrix. (**C**) Engineering stress-strain curves of PMMA-MW compared with pure PMMA. (**D**) SEM images of the fracture surfaces of PMMA-MW from the double-notch experiment, showing cracks containing nanofibrils ($\lambda_{PMMA\text{-}MW}$ ~5). (**E**) WAXS spectra of MW, PMMA, and PMMA-MW. The deconvoluted characteristic peak of MW in the PMMA matrix shows a slight shift to a lower *q*-vector, indicating an expansion of the MW's unit cell within the composite. (**F**) DSC curves of PMMA and PMMA-MW revealing an increase in T_g (~10°C). (**G**) Gel permeation chromatography traces of PMMA and PMMA-MW showing a decrease in PMMA molecular weight.

COF and slightly expand the unit cell of the woven COF crystals.

In differential scanning calorimetry (DSC) studies, we observed an ~10°C increase in the glass transition temperature (T_g) for PMMA when 3 wt % of MW nanocrystals were blended in (Fig. 2F). The DSC curves show only one transition, confirming the rather uniform phase behavior of PMMA within the detection resolution of the DSC technique. The uniform T_g transition suggests a long-range effect of the PMMA-COF interactions beyond the COF

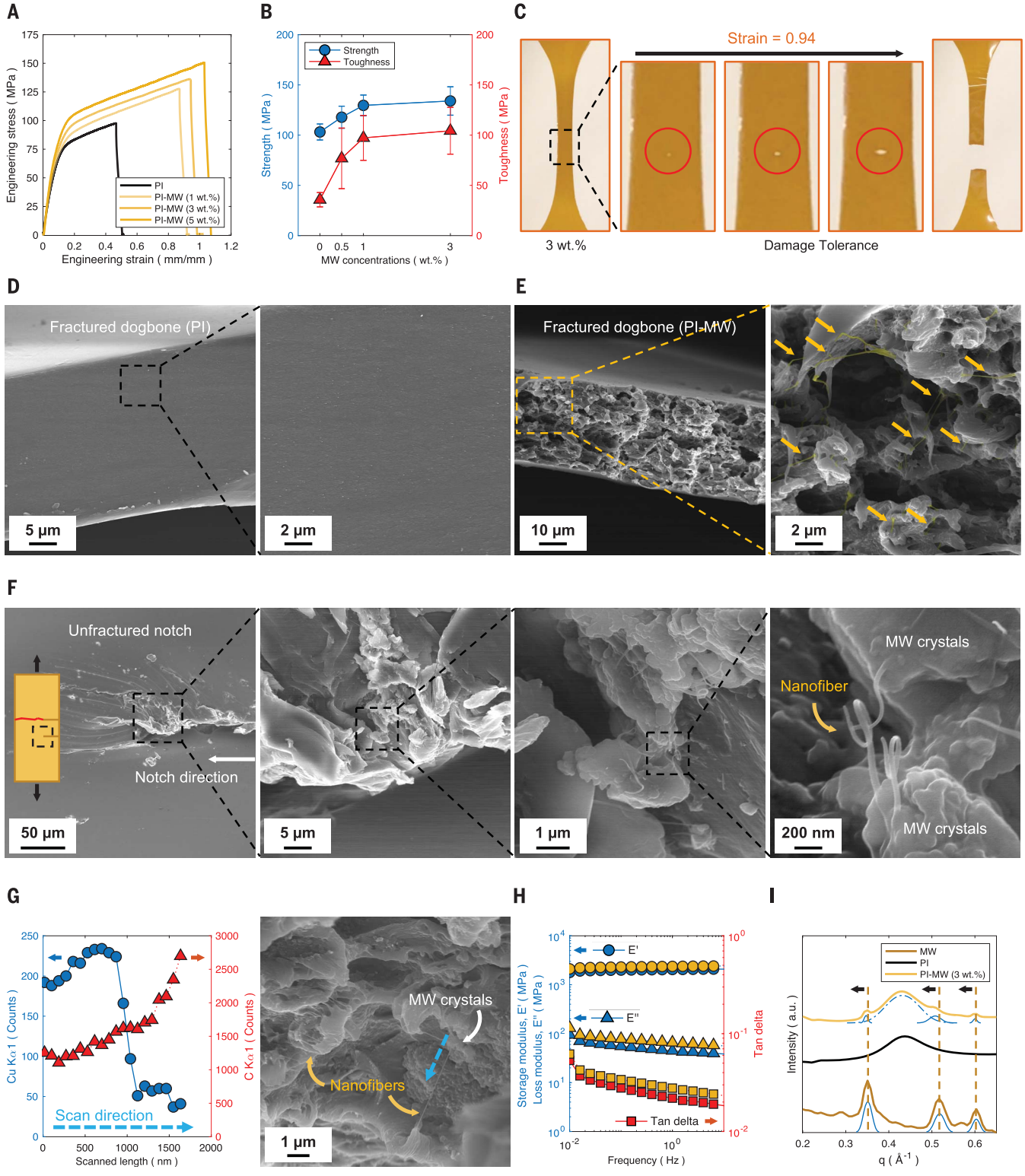

Fig. 3. PI-COF composites. (**A**) Engineering stress-strain curves of PI-MW composites compared with pure PI. (**B**) Comparison of stress and toughness in PI-MW composites as functions of filler concentration (n = 5 samples for each condition). (**C**) PI-MW (3 wt %) showing increased damage tolerance in the presence of a defect when the strain reaches ~0.94 mm/mm. (**D**) Fracture surface of pure PI showing almost no surface roughness in SEM images. (**E**) SEM images of fracture surfaces of the PI-MW showing high-aspect-ratio fibrils. (**F**) SEM images of the fracture surfaces of PI-MW from the double-notch experiment showing high-aspect-ratio nanofibrils in the unbroken notch. (**G**) EDX line scan of nanofibrils showing a transition in the chemical composition from PI-MW composite to pure PI. (**H**) Frequency-sweep dynamic mechanical analysis results showing enhanced viscoelastic properties when adding 3 wt % of MW (yellow). (**I**) WAXS studies comparing MW and PI-MW composites showing a slight peak shift to lower q-vectors.

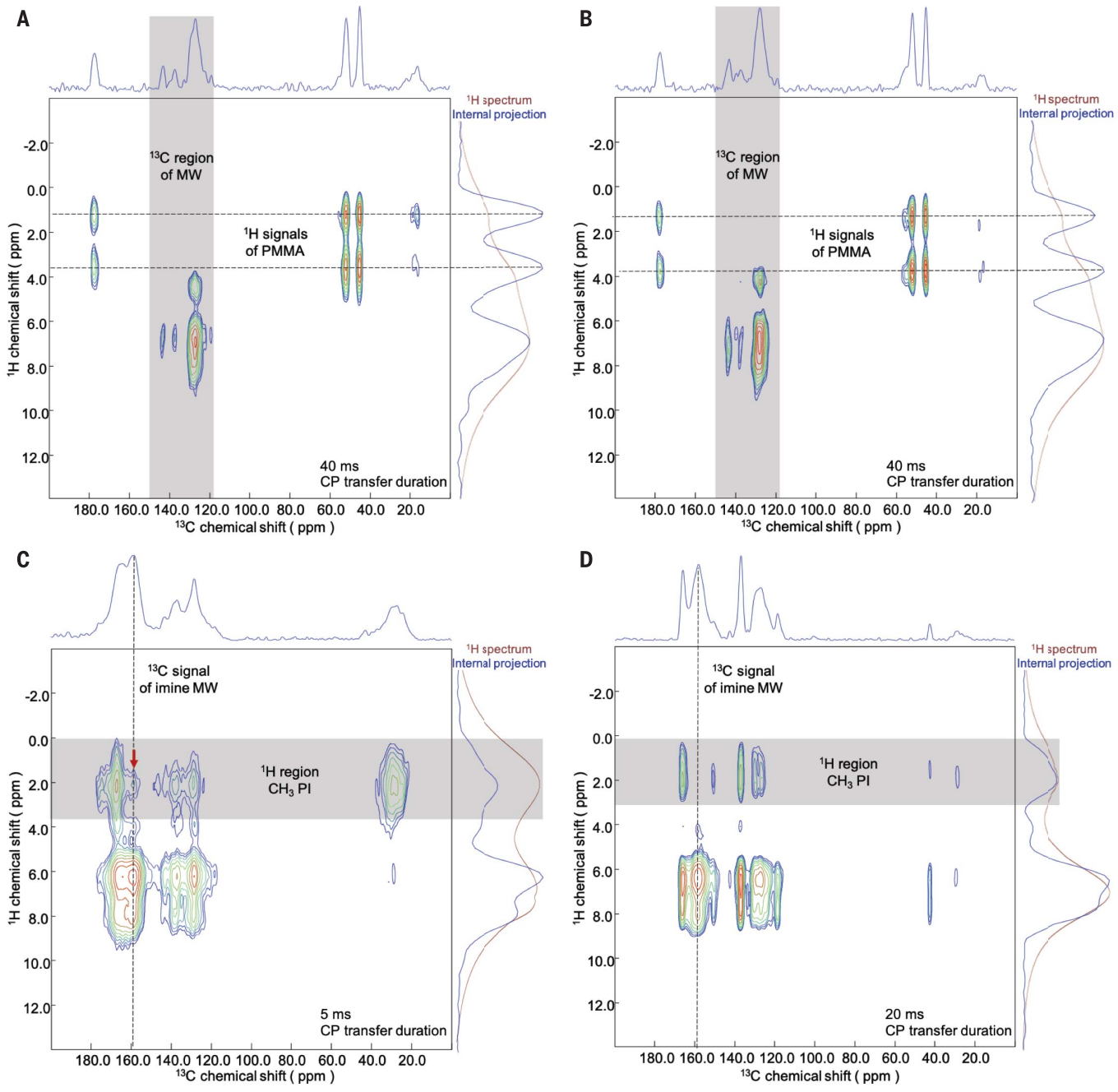

Fig. 4. Investigation of polymer-COF interactions by CP-HETCOR solid-state NMR spectroscopy. (**A** and **B**) ^{1}H-^{13}C CP-HETCOR NMR spectra of a PMMA-MW (20:80 by weight) composite (A) and a PMMA-MW (20:80 by weight) physical mixture (B) showing no correlation spots between the polymer and the COF at a contact time of 40 ms. (**C**) ^{1}H-^{13}C CP-HETCOR NMR spectrum of a PI-MW (50:50 by weight) composite showing a clear correlation spot (red arrow) between the polymer and the COF at a contact time of 5 ms. (**D**) ^{1}H-^{13}C CP-HETCOR NMR spectrum of a PI-MW (50:50 by weight) physical mixture showing no correlation spot between the polymer and the COF at a contact time of 20 ms.

crystal-PMMA interfaces. We measured the molecular weight of PMMA after dissolving the PMMA-MW composites and filtering out MW nanocrystals (Fig. 2G). Gel permeation chromatography spectra showed a reduction in the M_n of PMMA from 535.5 kDa (PDI = 2.50) to 433.2 kDa (PDI = 2.62). Despite the small changes and the high PDI of the PMMA matrices, the results were rather consistent among different runs (n = 3). Thus, higher M_n PMMA chains were likely trapped at the MW crystals and were removed from the solution during the filtration of MW nanocrystals, lowering M_n for the remaining solution.

PI-COF composites

PI, a liquid crystalline polymer, is chemically similar to the backbone of the woven COF nanocrystals. We selected PI to investigate the formation of polymer-COF junctions and their effect on the mechanical properties of the resulting composite. The PI-COF composites were synthesized by in situ polymerization of pyromellitic dianhydride (PMDA) and 4,4′-oxydianiline (ODA) in a blend of COF crystallites (see the supplementary materials, section S1).

Compared with pure PI, the PI-COF composites exhibited improved macroscopic mechanical properties, including strength, ductility, toughness, and damage tolerance (Fig. 3A). The incorporation of 0.5 to 1 wt % of MW resulted in a substantial increase in these properties, suggesting that the percolation threshold corresponded to very low filler ratios (~1 wt %) in PI-MW (Fig. 3B). At this concentration, the interparticle distances of PI-MW were ~1.7 (±1.2) μm, as determined from TEM analysis (see the supplementary materials, section S8). Collectively, these observations demonstrated that the effect of the polymer-COF junction extends beyond the range of filler-matrix interfaces, which is typically limited to tens of nanometers (*37*). Furthermore, the tensile tests on PI-MW showed enhanced fracture resistance even in the presence of a stress raiser in the form of surface imperfections, in marked contrast to the catastrophic ruptures observed in pure PI (Fig. 3C).

SEM fractography showed that the cross-sections of the fractured dog bone samples of pure PI had almost no detectible surface roughness (Fig. 3D). By comparison, the cross-sections of the PI-MW dog bones had higher surface roughness than pure PI dog bones (Fig. 3E). Over length scales of hundreds of micrometers, the PI-MW showed a homogeneous fracture surface roughness with no interface-initiated cavitation (see the supplementary materials, section S2). In addition, higher-magnification SEM images revealed highly anisotropic nanofibrils. Compared with the PMMA-COF composites, a large number of high-aspect-ratio nanofibrils [λ_{PI-MW} ~16.08 (± 8.67), $n > 10$ samples] bridging the MW crystal agglomerates were observed using double-notch fractographic techniques (Fig. 3F).

To investigate the chemical compositions of the observed nanofibrils, SEM energy-dispersive x-ray spectroscopy (EDX) was performed. The fibrils gradually transitioned from a combination of COF and PI to pure PI, as verified by a decrease in the copper content (wt %) from the origin of the craze fibrils to their tips (Fig. 3G). Furthermore, the addition of 3 wt % of MW led to a simultaneous enhancement in the storage and loss modulus of 15.8% (±0.3%) and 42.5% (±4.9%), respectively, for frequencies from 0.01 to 10 Hz (Fig. 3H), indicating that the composites underwent energy dissipation pathways. These results are consistent with the in situ formation of nanofibrils by unthreading the penetrated polymer strands that are spatially arranged through the nanometer-level periodicity of the COF nanocrystals.

To study the molecular interactions between the woven nanocrystals and the PI chains, the PI-COF composites were characterized by WAXS (Fig. 3I). The original scattering peaks from PI-MW (3 wt %) were deconvoluted and then compared with pristine MW because the characteristic peaks of MW were situated on the slope of the scattering peak from PI. WAXS results of PI-MW showed a slight unit cell expansion of MW, similar to what had been observed with the PMMA-MW composites.

Further characterization of the fibril formation capability by polymer unthreading in response to mechanical force was performed by WAXS studies on the plastically deformed PI-MW films (see the supplementary materials, section S9). The stretching process oriented the composite in the force direction without affecting the structure of the COF crystals. Azimuthal integration at $q = 0.439$ Å^{-1}, which represents the intramolecular spacing of neat PI (*38*), was conducted to show the orientation of the polymer chains in each system. The PI-MW composites (3 wt %) showed a higher orientational order parameter $\bar{P}_2$, estimated from the azimuthal integration (*39*), as indicated by the increased intensity variation. We concluded that the intramolecular distance of the PI chains was more uniform in PI-MW compared with PI, further supporting our polymer-COF junction hypothesis.

To delineate the contribution of covalent bond formation between the polymer and the COFs, additional tensile tests were performed (see the supplementary materials, section S10). In these experiments, the PI-MW films were prepared by the physical mixing of COFs into poly(amic acid) solutions and by in situ polymerization using the surface-passivated COFs. In both experiments, reactions between the monomers and the surface functional groups of the COFs were eliminated (see the supplementary materials, section S11). The tensile test results showed that the strength and toughness of the PI-MW composites were still effectively improved compared with pure PI films. This provides evidence that topological, noncovalent entanglements between the COF crystals and polymer matrix played a greater role than covalent bonding in improving the mechanical properties of PI-MW composites.

Elucidation of polymer-COF junctions

To investigate the possibility of PI chains threading through the pores of the COF, the uptake of the monomers was investigated by monomer inclusion studies (see the supplementary materials, section S7). MW nanocrystals were soaked in a solution of the molecule of interest, such as PMDA or ODA, followed by extensive washing steps to eliminate excess monomers outside of the pores. The amount of monomer inside the pores of the COFs was quantified by digest NMR spectroscopy, in which the COF material was broken down into its building blocks by acid digestion before NMR analysis. The digest NMR spectra of the soaked and subsequently washed COFs showed signals consistent with the monomers within the pores, further substantiating that the monomers could diffuse into the pores of MW.

Further insight into the nature of the polymer-COF interactions was gained through 2D solid-state NMR using cross polarization-based heteronuclear correlation (CP-HETCOR) spectroscopy. This technique allowed us to probe the intermolecular proximities between the backbone of the COF and the polymer threads of PMMA and PI. Previous studies have shown different correlations between surface interactions and polymer threading in polymer-MOF systems (*40*). Here, we compared PMMA-MW and PI-MW samples with physical mixtures of the polymers and MW. This technique requires sufficient resolution in both the ^{1}H and ^{13}C dimension, as well as the presence of a unique correlation spot arising from a heteronuclear pair between the polymer and the COF. In the case of PMMA-COF composites, the proton and carbon signals of the methyl and methoxy groups in the PMMA were easily distinguishable from the mostly aromatic backbone of the COF. CP-HETCOR experiments of PMMA-MW composites and physical mixtures with long CP-transfer durations, also called contact times, of 40 ms showed no correlation between carbon and proton signals of the COF and PMMA, thereby indicating that the polymer was not in close proximity to the woven nanocrystals (Fig. 4, A and B). These results provide evidence for a polymer-COF system that is dominated by surface interactions, in which most of the polymer strands did not interact substantially with the pores of the COF.

Similar investigations of PI-MW composites posed a greater challenge because both the polymer and the COF overlapped in their ^{1}H and ^{13}C NMR spectra. To overcome this, the chemical backbone of the two components was adjusted to generate a heteronuclear pair between PI and MW with distinct ^{1}H and ^{13}C chemical shifts. To incorporate a well-resolved ^{1}H signal, ODA was replaced by a common monomer in polyimide synthesis, 4,4'-(propane-2,2-diyl)dianiline. The methyl groups introduced a proton signal with a chemical shift of ~1.5 ppm, which was distinct from the mostly aromatic footprint of the PI-MW composites. To improve both resolution and sensitivity in the carbon dimension, the ^{13}C-enriched imine-linked variant of the woven COF was used in these studies, which ultimately led to a detectable PI-MW correlation spot between the methyl protons and the enriched imine carbon.

In contrast to PMMA-MW, the HETCOR spectrum of PI-MW composites showed a clear correlation spot for the heteronuclear pair of the enriched imine carbon in the COF and the methyl protons in the polymer at a relatively short contact time of 5 ms (Fig. 4C). Shorter CP contact times probe shorter distances, thereby indicating intimate mixing between the polymer

strands and the woven framework, which is indicative of polymer threading. By comparison, no such correlation spot was observed for the physical mixture of preformed PI and MW, even at substantially longer contact times of 20 ms (Fig. 4D).

Discussion

The results presented in this work demonstrate that woven COF nanocrystals can interact with polymers to generate mechanically enhanced composites. Depending on the mechanical and chemical similarity of the COF backbone and the polymer matrix, the interactions may be limited to the interface or lead to a threading of polymer strands through the pores of the woven framework. Spectroscopy studies substantiate the evidence for the formation of polymer-COF junctions in PI-MW composites, whereas interactions in PMMA-MW are likely limited to interfacial entanglements. This mechanistic difference in polymer-COF interactions is supported by the extent of the mechanical property enhancement between PI and PMMA, as well as the morphology of the unthreaded nanofibrils ($\lambda_{PI-MW} > \lambda_{PMMA-MW}$). In contrast to other MOFs and COFs, the woven backbone exhibits superior compatibility with the polymer matrices, leading to excellent filler distribution and good mechanical performance.

REFERENCES AND NOTES

1. S. F. Edwards, *Proc. Phys. Soc.* **92**, 9–16 (1967).
2. G. Allen, A. Charlesby, D. Tabor, G. N. Welding, *Proc. R. Soc. London Ser. A* **351**, 381–396 (1976) [and Discussion].
3. J. H. Koo, *Fundamentals, Properties, and Applications of Polymer Nanocomposites* (Cambridge Univ. Press, 2016).
4. M. R. Bockstaller, R. A. Mickiewicz, E. L. Thomas, *Adv. Mater.* **17**, 1331–1349 (2005).
5. H. S. Varol *et al*., *Proc. Natl. Acad. Sci. U.S.A.* **114**, E3170–E3177 (2017).
6. W. W. Graessley, D. S. Pearson, *J. Chem. Phys.* **66**, 3363–3370 (1977).
7. J. Kim, G. Zhang, M. Shi, Z. Suo, *Science* **374**, 212–216 (2021).
8. L. Brunsveld, B. J. B. Folmer, E. W. Meijer, R. P. Sijbesma, *Chem. Rev.* **101**, 4071–4098 (2001).
9. S. K. Kumar, N. Jouault, B. Benicewicz, T. Neely, *Macromolecules* **46**, 3199–3214 (2013).
10. J. Choi *et al*., *Langmuir* **29**, 6452–6459 (2013).
11. J. Xu *et al*., *Science* **355**, 59–64 (2017).
12. S. Rose *et al*., *Nature* **505**, 382–385 (2014).
13. J. Choi *et al*., *Soft Matter* **8**, 4072–4082 (2012).
14. M. Rubinstein, A. V. Dobrynin, *Curr. Opin. Colloid Interface Sci.* **4**, 83–87 (1999).
15. S. Zhu *et al*., *Nat. Commun.* **15**, 118 (2024).
16. P. G. De Gennes, in *Microscopic Aspects of Adhesion and Lubrication, Proceedings of the 34th International Meeting of the Société de Chimie Physique, 14–18 September 1981*, J. M. Georges, Ed. (Elsevier, 1981), Tribology Series, vol. 7, pp. 355–367.
17. Z. O. G. Schyns, M. P. Shaver, *Macromol. Rapid Commun.* **42**, e2000415 (2021).
18. P. G. de Gennes, *J. Chem. Phys.* **55**, 572–579 (2003).
19. Y. Liu *et al*., *J. Am. Chem. Soc.* **141**, 677–683 (2019).
20. Y. Liu *et al*., *Science* **351**, 365–369 (2016).
21. Y. Liu *et al*., *J. Am. Chem. Soc.* **140**, 16015–16019 (2018).
22. T. Ma *et al*., *J. Am. Chem. Soc.* **140**, 6763–6766 (2018).
23. H. L. Nguyen, C. Gropp, Y. Ma, C. Zhu, O. M. Yaghi, *J. Am. Chem. Soc.* **142**, 20335–20339 (2020).
24. J. Jiang *et al*., *J. Am. Chem. Soc.* **136**, 12844–12847 (2014).
25. T. Loiseau *et al*., *Chemistry* **10**, 1373–1382 (2004).
26. B. Lee, Z. Niu, S. L. Craig, *Angew. Chem. Int. Ed.* **55**, 13086–13089 (2016).
27. M. Zhang, G. De Bo, *J. Am. Chem. Soc.* **141**, 15879–15883 (2019).
28. M. Zhang, G. De Bo, *J. Am. Chem. Soc.* **142**, 5029–5033 (2020).
29. C. S. Diercks, O. M. Yaghi, *Science* **355**, eaal1585 (2017).
30. P. J. Waller, F. Gándara, O. M. Yaghi, *Acc. Chem. Res.* **48**, 3053–3063 (2015).
31. F. Haase, B. V. Lotsch, *Chem. Soc. Rev.* **49**, 8469–8500 (2020).
32. P. J. Waller *et al*., *J. Am. Chem. Soc.* **138**, 15519–15522 (2016).
33. P. Novak, R. Yuan, B. P. Somerday, P. Sofronis, R. O. Ritchie, *J. Mech. Phys. Solids* **58**, 206–226 (2010).
34. R. K. Nalla, J. H. Kinney, R. O. Ritchie, *Nat. Mater.* **2**, 164–168 (2003).
35. E. J. Kramer, in *Advances in Polymer Science*, H. H. Kausch, Ed. (Springer, 1983), *Crazing in Polymers* vol. 52/53, pp. 1–56.
36. A. M. Donald, E. J. Kramer, *J. Polym. Sci., Polym. Phys. Ed.* **20**, 899–909 (1982).
37. H. K. Nguyen, K. Nakajima, *Macromolecules* **55**, 2739–2745 (2022).
38. J.-H. Jou, P.-T. Huang, *Polym. J.* **22**, 909–918 (1990).
39. G. Weng, G. Huang, L. Qu, Y. Nie, J. Wu, *J. Phys. Chem. B* **114**, 7179–7188 (2010).
40. P. Duan *et al*., *J. Am. Chem. Soc.* **141**, 7589–7595 (2019).

ACKNOWLEDGMENTS

We thank W.-C. Liao and A. Lund for assisting with the collection of solid-state NMR data. **Funding:** This work was funded by the Defense Advanced Research Projects Agency under contracts HR001119S0048 and HR00112290097. We acknowledge the College of Chemistry Nuclear Magnetic Resonance Facility for resources and staff assistance, where the instruments are supported by the National Science Foundation under grant no. 2018784. We thank the University of California Berkeley Electron Microscope Laboratory (EML) for access and assistance in electron microscopy data collection. Wide-angle X-ray scattering studies were performed at the Advanced Light Source, which is supported by the U.S. Department of Energy, Office of Science (DE-AC02-05CH11231). C.G., a Leopoldina postdoctoral fellow of the German National Academy of Science (LPDS 2019-02), acknowledges the receipt of a fellowship from the Swiss National Science Foundation (P2EZP2-184380). N.H. thanks the Studienstiftung des deutschen Volkes and acknowledges receipt of the KAVLI ENSI Philomathia Graduate Student Fellowship and Blavatnik Innovation Fellowship. T.X., J.K., and T.C. are partially supported by the US Department of Energy, Office of Science, Office of Basic Energy Sciences, Materials Sciences and Engineering Division, under contract DE-AC02-05CH11231 (Organic-Inorganic Nanocomposites KC3104). **Author contributions:** S.E.N., C.G., O.M.Y., and T.X. conceived the idea. O.M.Y., T.X., S.E.N., and J.K. led the project. S.E.N. synthesized the COFs, developed postsynthetic methodologies, and conducted the spectroscopic (IR and NMR), thermal gravimetric analysis, solid-state NMR, and elemental analysis characterizations. J.K. synthesized polymer-COF composites and conducted mechanical property measurements and characterizations (SEM fractography, Nano DMA, double-notch fracture test, and nanoindentation). C.G. performed monomer inclusion studies. T.M. supported the synthesis COFs and performed SEM experiments. N.H. conducted sorption experiments. L.M. performed WAXS studies and TEM. S.J. and T.C. supported the polymer sample preparation and mechanical testing. R.G. designed and performed solid-state NMR experiments. K.W. supported the characterization by solid-state NMR. S.E.N., C.G., J.K., T.X., R.O.R., and O.M.Y. interpreted the results. S.E.N., J.K., T.X., R.O.R., and O.M.Y. wrote and reviewed the manuscript. **Competing interests:** S.E.N., J.K., C.G., T.X., and O.M.Y. are inventors on a patent application submitted by the University of California-Berkeley that covers molecular weaving additives to enhance the mechanical properties of materials. The remaining authors declare no competing interests. **Data and materials availability:** Synthetic procedures, spectroscopic (IR and NMR), thermal gravimetric analysis, x-ray diffraction data, mechanical testing results, and WAXS data reported in this manuscript are present in the main text or the supplementary materials.

SUPPLEMENTARY MATERIALS

science.org/doi/10.1126/science.adf2573
Materials and Methods
Supplementary Text
Figs. S1 to S30
Table S1
References (*41*–*45*)
Movies S1 and S2

Submitted 9 October 2022; resubmitted 23 October 2023
Accepted 14 February 2024
10.1126/science.adf2573